UCLA
UCLA Previously Published Works

Title

Understanding How Bonding Controls Strength Anisotropy in Hard Materials by Comparing the High-Pressure Behavior of Orthorhombic and Tetragonal Tungsten Monoboride

Permalink

Journal

ISSN

Authors

Lei, Jialin
Yeung, Michael T
Robinson, Paul J
et al.

Publication Date

DOI

Peer reviewed

High pressure studies of hard materials: volume deformation and strength anisotropy in orthorhombic and tetragonal tungsten monoboride under non-hydrostatic compression

Jialin Lei,[1] Michael T. Yeung,[1] Paul J. Robinson,[1] Reza Mohammadi,[3] Christopher L. Turner,[1] Jinyuan Yan,[5] Abby Kavner,[6] Anastassia N. Alexandrova,[1,4,*] Richard B. Kaner,[1,2,4,*] and Sarah H. Tolbert [1,2,4,*]

[1]Department of Chemistry and Biochemistry, UCLA, Los Angeles, California, 90095-1569 USA
[2]Department of Materials Science and Engineering, UCLA, Los Angeles, California, 90095 USA
[3]Department of Mechanical & Nuclear Engineering, Virginia Commonwealth University, Richmond, Virginia 23284, USA
[4]California NanoSystems Institute (CNSI), UCLA, Los Angeles, California, 90095 USA
[5]Advanced Light Source, Lawrence Berkeley National Lab, Berkeley, California 94720, USA
[6]Department of Earth and Space Sciences, UCLA, Los Angeles, California, 90095 USA

*Corresponding Authors: tolbert@chem.ucla.edu, kaner@chem.ucla.edu, ana@chem.ucla.edu

Abstract

In this work, we investigate the high pressure behavior of the stabilized high-temperature (HT) orthorhombic phase of WB using radial X-ray diffraction in a diamond-anvil cell at room temperature. The experiments were performed under non-hydrostatic compression up to 52 GPa. For comparison, the low temperature (LT) tetragonal phase of WB was also compressed non-hydrostatically to 36 GPa to explore structurally-induced changes to its mechanical properties. Although our microindentation hardness tests indicate that the HT WB possesses slightly higher hardness, synchrotron-based high-pressure compression data yield significant distinct incompressibilities. The ambient pressure bulk modulus of the HT phase of WB is 341 ± 5 GPa obtained by using the second order Birch-Murnaghan equation-of-state, while for the LT phase of WB the incompressibility increased to 381 ± 3 GPa. The elastically-supported differential stress was

measured in a lattice specific manner and analyzed by using lattice strain theory. Greater strength anisotropy was observed in the HT WB phase, compared to the LT materials. DFT energy shift calculations indicate that W-B bonds, rather than B-B bonds are responsible for the lattice-dependent mechanical properties.

Introduction

As the world's hardest natural material, diamond has surprisingly limited applications in cutting and drilling, since it reacts with ferrous materials to form brittle carbides.[1,2] With an increasing demand for diamond replacements, many superhard materials have been discovered with both good chemical stability as well as high hardness, including rhenium diboride (ReB_2), and cubic boron nitride (c-BN).[3,4,5] Unfortunately, synthetic requirements for c-BN (*i.e.* high pressure and high temperature) lead to high costs, limiting its use. Similarly, use of ReB_2 is limited because it contains an expensive platinum group metal. Tungsten tetraboride (WB_4) has emerged as a less expensive superhard material. WB_4 has a Vickers hardness that reaches 43.3±2.9 GPa[6,7] under an applied load of 0.49 N and a bulk modulus of 324±3 GPa.[8] Its high hardness results from the high valence electron density of tungsten and short strong covalent bonds introduced by boron. However, it is still a challenge to make phase pure WB_4. As a thermodynamically unfavorable phase, WB_4 cannot be made by high temperature arc melting unless the W:B molar ratio is kept at 1:12.[9] The WB_4 samples prepared in this way are therefore not stoichiometric, but rather a

composite of WB_4 and crystalline boron, which introduces unwanted non-uniformity.[10,11]

Lower borides of transition metals may offer a solution to the stoichiometry problem if superhard phases can be found. In particular, consider tungsten monoboride (WB), with a tungsten-tungsten bond distance of 2.8 Å that is comparable to pure tungsten metal (2.7 Å). This similarity with pure tungsten suggests a stronger metallic character than any of the previously mentioned borides, bringing with it the ductility and electrical conductivity typically found in conventional metals.

Tungsten monoboride possesses two distinct phases with a B:W molar ratio of 1:1,[12] one orthorhombic high temperature (HT) phase and one tetragonal low temperature (LT) phase with a transition temperature of 2170 °C. Both of these phases share the same alternating BCC tungsten bilayer/boron chain superstructure, but differ in the arrangement of the boron atoms. In the LT-tetragonal phase, the boron chains alternate to form perpendicular arrays, but in the HT-orthorhombic phase, the boron chains are all aligned along the c-axis and this is responsible for the subtle orthorhombic distortion (**Fig. 1**). It has been reported that LT tetragonal WB is an ultra-incompressible material[13] with a bulk modulus of 428 – 452 GPa[14,15] and a maximum differential stress of 14 GPa, suggesting it could be a potential candidate for a superhard material. However, due to the synthetic challenges in stabilizing a high temperature phase, no high pressure study

has yet been carried out on the HT-orthorhombic phase of WB. Fortunately, in our recent study,[16] it has been demonstrated that by doping a small amount of Ta into WB, the HT orthorhombic phase of WB can be stabilized at room temperature. According to our Vickers micro-indentation hardness measurement, the hardness of HT-orthorhombic WB (35.5 ±2.5 GPa) is higher than the hardness of LT-tetragonal WB (31 ± 3.0 GPa), a result that is not obvious from the differences in crystal structure, particularly if one postulates that the network of B-B bonds should dominate the hardness. In that case, the more isotropic network in the LT WB would be expected to result in a harder material. Moreover, the elastic deformation behavior such as bulk modulus and crystal lattice strain response to an applied non-hydrostatic stress of this new metallic metal boride have not been characterized. Most importantly, the ability to examine two different tungsten monoboride phases that differ only in the arrangement of the boron chains should provide an excellent model system to understand the extent to which boron chain dimensionality controls lattice deformations.

Here, synchrotron-based angle dispersive X-ray diffraction (XRD) experiments in a radial geometry using a diamond anvil cell (DAC)[17] were performed to examine the volumetric deformations and anisotropic lattice deformations of orthorhombic and tetragonal WB under uniaxial applied pressures up to 52 GPa and 36 GPa, respectively. While the anisotropic stress condition in the DAC during compression in the radial experimental geometry,[18,19,20] is different to that under an indenter's tip in a micro-

indentation hardness test,[21] there are enough similarities that this data can provide insights for understanding the microscopic response of a crystal lattice to differential stress and thus to understanding the macroscopic response to an applied load. Additionally, radial XRD enables us to make *in situ* observations of deformation behavior in a lattice specific manner as a function of pressure.

Experimental procedure

Orthorhombic and tetragonal WB were synthesized by arc melting. Tungsten powder and boron powder with a 1:1 molar ratio were mixed together followed by pressing into pellets. Subsequently, the pellets were arc melted and cooled in argon gas. More synthetic details can be found in Ref. 16. In order to stabilize the HT-orthorhombic phase of WB at room temperature, 5 at.% Ta was added because TaB is known to crystallizes in the orthorhombic structure. Tetragonal WB and orthorhombic stabilized WB pellets were then crushed and ground with a Plattner's-style hardened tool-steel mortar and pestle set (Humboldt Mfg., Model H-17270). The fine powder (<20 μm) was obtained by sieving with a No. 635 mesh sieve (Humboldt Mfg.). We performed non-hydrostatic *in situ* high pressure angle-dispersive X-ray diffraction experiments to characterize the strength and deformation behavior at synchrotron beamline 12.2.2 of the Advanced Light Source (ALS, Lawrence Berkeley National Lab). A polycrystalline WB sample was loaded into a laser drilled hole (~60 μm in diameter) in a boron gasket

(~400 μm in diameter and ~70 μm in thickness) made of amorphous boron and epoxy.[22] A small circle of Pt foil (~15 μm in diameter) was placed on top of the sample to serve as an internal pressure standard. No pressure-transmitting medium was used in order to create a non-hydrostatic environment in the DAC. More technical details for the DAC can be found in Ref. [23]. A monochromatic X-ray beam with a wavelength of 0.4959 Å, and a spot size of 20×20 μm was passed through the sample perpendicular to the loading axis. The 2D diffraction image was collected using an MAR-345 image plate at steps of ~4 GPa. Calibration of the detector distance and orientation used a LaB_6 standard and the program FIT2D.[24] The ring-like diffraction patterns were "unrolled" into cake diffraction patterns, a plot of azimuthal angle η (with 0° and 180° the low stress directions and 90° and 270° the high stress directions) versus 2θ (**Fig. S1**), followed by importing into Igor Pro (WaveMetrics, Inc.), where diffraction lines were analyzed individually. The combination of radial X-ray diffraction and lattice strain theory[25,26,27] enable us to study the stress state of samples under non-hydrostatic compression in a DAC.

The stress state in a compressed sample under uniaxial loading in a DAC is characterized by σ_3, the maximum stress along the axial direction, and σ_1, the minimum stress in the radial direction. The difference between σ_1 and σ_3 is the macroscopic differential stress t, which can be defined by the Tresca yield criterion:

$$t = \sigma_3 - \sigma_1 \le 2\tau = \sigma_y, \qquad (1)$$

where τ is the shear strength and σ_y is the yield strength of the material.[28] A measurement of the elastically-supported differential stress thus enables one to estimate the lower-bound of the material's yield strength, σ_y.

According to lattice strain theory, the measured d-spacing, $d_m(hkl)$ is a function of $d_p(hkl)$, the d-spacing under the hydrostatic pressure, and φ, the angle between the diffracting plane normal and the maximum stress axis,

$$d_m(hkl) = d_p(hkl)\left[1 + \left(1 - 3\cos^2\varphi\right)Q(hkl)\right], \quad (2)$$

where $Q(hkl)$ is the orientation dependent lattice strain,[29] which is defined by

$$Q(hkl) = \left(\frac{t}{3}\right)\left\{\alpha\left[2G_R(hkl)\right]^{-1} + (1-\alpha)\left(2G_V\right)^{-1}\right\}. \quad (3)$$

Here $G_R(hkl)$ is the lattice dependent Reuss shear modulus under iso-stress[30] conditions, while the Voigt shear modulus, G_V, is independent of hkl under iso-strain[31] conditions. The G_V is given by[32]

$$15G_V = \left(c_{11} + c_{22} + c_{33}\right) - \left(c_{12} + c_{23} + c_{31}\right) + 3\left(c_{44} + c_{55} + c_{66}\right). \quad (4)$$

For orthorhombic and tetragonal systems, the expressions of $G_R(hkl)$ in terms of elastic compliance $[S_{ij}]$, can be found in Ref. 27. The actual shear modulus of a randomly oriented polycrystalline sample is neither $G_R(hkl)$ nor G_V, but some weighted average of them, given by α. Approximately, the differential stress can be given by[25]

$$t = 6G<Q(hkl)>, \qquad (5)$$

where $<Q(hkl)>$ stands for the average value of lattice strain observed for the diffraction peaks and G is the aggregate shear modulus. According to Eq. (2), one should find that $d_m(hkl)$ is a linear function of $(1-3\cos^2\varphi)$ with a slope of $d_p(hkl)Q(hkl)$ and an intercept of $d_p(hkl)$ (with $x=0$ corresponding $\varphi=54.7°$). The $Q(hkl)$ resolved from the slope can be used to evaluate and describe contributions of both plastic and elastic deformation.[33,34]

The pressure dependent *d-spacing* at $\varphi=54.7°$ reflects compression behavior due to the hydrostatic component of stress; as a result, the equivalent hydrostatic compression curve can be derived from non-hydrostatic data at the magic angle. The zero pressure bulk modulus, K_0, can then be determined by fitting the compression curve to the Birch-Murnaghan equation-of-state (EOS),[35]

$$P = 1.5 K_0[(V/V_0)^{-7/3} - (V/V_0)^{-5/3}]. \quad (6)$$

Here, the pressure, P, and the unit cell volume, V, are measured at $\varphi=54.7°$.

Results and discussion

The high pressure compression experiments in a radial geometry were performed on HT-orthorhombic WB and LT-tetragonal WB, respectively. The HT-orthorhombic WB was compressed up to 52 GPa and the diffraction

patterns were collected at steps of ~4 GPa. Representative XRD patterns for HT-orthorhombic WB are shown in **Fig. 1a**. The stick reference pattern below the experimental diffraction peaks is from the Joint Committee on Powder Diffraction Standards (JCPDS Card #00-006-0541). A clear shift towards higher angles with increasing pressure can be seen due to the decreased lattice constants. Note that no Ta peaks appear in the pattern across the entire pressure range, meaning the added Ta indeed forms a solid solution with the W, *i.e.* $Ta_{0.05}W_{0.95}B$, and the dopants do not precipitate into an X-ray observable unique phase during compression. While solid solution formation may influence mechanical properties, considering the low doping amount and the small difference in atomic size (~5%) between Ta (1.49 Å) and W (1.41 Å),[36] we believed that changes in mechanical properties due to the difference in crystal structural (orthorhombic *vs.* tetragonal) will likely dominate over changes that arise from chemical doping. The LT-tetragonal WB was compressed up to 36.4 GPa and its representative XRD patterns are shown in **Fig. 1b**. The pressure at each point was determined at $\varphi=54.7°$ by fitting the equation-of-state of Pt[37] to its lattice parameter.

The pressure dependence of *d*-spacings and lattice constants are summarized in **Fig. 2** and **Table S1**. There are no signs of phase transformations upon compression. For HT-orthorhombic WB, we chose to study the diffraction planes (200), (020) and (002). These three orthogonal planes reflect the anisotropic deformation behavior of lattice constants *a*, *b* and *c*. As LT WB is tetragonal, and so the (200) and (020) lattice planes are

symmetry related. We thus chose to study the (200) and (004) diffraction planes to capture the unique lattice constants of the LT WB. Figure 3 shows the dependence of the d-spacings as a function of $\left(1-3\cos^2\varphi\right)$ for the selected planes at the highest pressure, which shows the expected linear variation according to Eq. (2). The slope of each line gives the corresponding $Q(hkl)$ and the intercept yields the d-spacing under the mean normal stress. According to Equation 3, this value can be directly related to the ratio of the differential stress to aggregate shear modulus (t(hkl)/G) and can be termed the differential strain. Values of t/G for the HT-orthorhombic WB (black) and LT-tetragonal WB (red) are plotted as a function of pressure in **Fig. 4a**. As one might expect from the lower symmetry crystal structure, the HT-orthorhombic WB shows larger variations in the t(hkl)/G ratio than the LT-tetragonal WB phase across different lattice constants, which is an indication of higher elastic anisotropy in differential strain. This likely arises from the difference in crystal structure between the HT-orthorhombic phase and the LT-tetragonal phase. When comparing their structures **(Fig. 1)**, we note that all the boron zigzag chains are in the same direction in the HT-orthorhombic phase, while they are along the perpendicular directions in the LT-tetragonal phase.

For HT-orthorhombic WB, the t(200)/G ratio shows an almost linear variation with pressure achieving the highest value of 4.7% at 52 GPa. No plateau is observed, indicating that the elastic limit is not reached during the course of this experiment. As a result, any differential stress data calculated

from this strain data need to be considered as a lower bound on the materials strength.

By contrast, the t(020)/G ratio increases linearly with pressure at the beginning, but then levels off and increases more slowly above ~15 GPa, ending with a plateau value of 4.4% at ~26 GPa. The plateau is an indication of the onset of plastic deformation by a slip system.[33] As shown in **Fig. 1**, the (020) of HT-orthorhombic WB is equivalent to the (004) of LT-tetragonal WB, which is the plane parallel to the metal bilayers. The metal-metal bonds are likely weaker than the metal-boron and boron-boron bonds.[38] In addition, the theoretical C_{44} value is also smaller than the C_{55} and $C_{66,}$ confirming that the metal bilayer is the easy slip plane.[39] Therefore, it appears that at pressures higher than 15 GPa, the (020) plastically deforms and starts to slip.

Diffraction profile analysis was conducted to confirm this assumption. One important source for broadening of the peaks in high pressure experiments is the inhomogeneous strain caused by the local deviatoric stresses among crystallites under non-hydrostatic compression.[40,41] Figure 4b displays the evolution of the (020) peak broadening as a function of pressure, and we see a similar trend to that observed for $t(020)/G.$ The peak broadening in the linear regime mainly results from the inhomogeneous elastic strain. Upon further compression, it deviates from linearity and approaches a limiting value of ~0.17°, indicating that no more local stress can be stored in the crystallite and it has relaxed by slipping. The data with

open symbols at 0 GPa were taken upon decompression. The irreversible peak broadening reflects the residual stress effect in the quenched sample, which also suggests the sample deformed plastically under non-hydrostatic compression.

The data for *t(002)/G*, also shown in **Fig. 4a**, are somewhat more complicated. The differential strain is small, so the variation is close to the error in the values. It appears that this peak might presents a plateau in the 20-40 GPa range, but after that it resumes increasing, a finding that has not been observed in more covalent borides such as WB_4 and ReB_2.[42] Such behavior, if it is real, may arise from strain hardening effects. Alternatively, *t(002)/G* may simply increase across the entire pressure region, similar to *t(200)/G*. Considering that the elastic regime for both the (200) and (002) peaks of HT WB is quite large, the HT-orthorhombic tungsten monoboride may bring the very desirable property of reduced brittleness to the superhard materials family. It is interesting to consider the optimal balance between reduced brittleness and high hardness for various applications and how to design this into a material's system. It is logical that lower borides could show enhanced reduced brittleness because of their higher metal content.

Interesting, extended linear behavior without the onset of plastic deformation was not observed in the LT-tetragonal WB in **Fig. 4a**, which suggests that the arrangement of boron chains play an important role in

governing the onset of plastic deformation. As one might expect from the more isotropic crystal structure of the LT WB, the LT-tetragonal phase is more isotropic in differential strain compared to HT WB. The data for the (004) plane (which is analogous to the (020) plane for the HT phase) show similar behavior to the HT (020) plane. There is a plateau in both the t/G ratio (**Fig. 4a**) and the FWHM (**Fig. 4b**) at ~20 GPa, suggesting that the (004) plane starts to slip at ~20 GPa. What is unexpected is that despite the orthogonal network of boron chains, the LT (200) plane shows nearly identical behavior to the (004) with $t(200)/G$ first increasing linearly and then plateauing above ~20 GPa. The LT phase of WB thus does not show the reduced brittleness observed in HT WB.

Unlike the differential strain, the differential stress (t) can be directly correlated to hardness. The differential stress under Reuss and Voigt conditions for HT-orthorhombic WB and LT-tetragonal WB was calculated by using the elastic stiffness constants calculated in Ref. [43] and Ref. [44], respectively. While the real differential stress is some weighted average of these two conditions, the correct weighting for our experimental conditions is not known, so we simply calculate both values as upper and lower limits on the actual values. As shown in **Fig. 5**, the anisotropic nature of HT WB is preserved under both conditions. The plateau in the differential stress supported by the (020) plane suggests that it has reached its actual yield strength (9-11 GPa) at pressures achieved in this experiment. In contrast, the $t(200)$ shows no plateau across the pressure range under both

13

conditions; therefore, we cannot estimate its corresponding yield strength. However, considering that the (200) plane supported the highest value (11-13 GPa) among the selected planes at 52 GPa, we can conclude that its true yield strength should be even higher, indicating that the *a* axis is the hardest direction, followed by the *b* axis, the ultimate plateau value for the *c* axis remaining difficult to estimate.

Some insight into the difference in behavior between the LT tetragonal phase and the HT orthorhombic phase can be obtained from simple symmetry considerations. There are only two possible slip systems for an orthorhombic crystal:[45] <100>{010} and <001>{010}. Given that *t(200)* is much higher than *t(002)*, it is very likely that <001>{010} is the most active and dominant slip system under the experimental conditions. By contrast, the tetragonal crystal structure has 6 slip systems (<001>{100}, <011>{110}, <111>{1-10}, <10-1>{101}, <111>{11-2} and <10-1>{121}). These symmetry constraints may explain, at least in part, why the plateau pressure of the LT tetragonal (200) plane is only 20 GPa, while the HT orthorhombic (200) and (002) planes still have not plateaued at pressures above 50 GPa. The availability of suitable slip systems may allow for a much lower onset of plastic deformation in the LT tetragonal phase.

In order to gain further insights into strength anisotropy, particularly for the HT orthorhombic phase of WB, we turn to DFT calculations. All details on the calculation methods can be found in the SI. There are three basic types

of bonds in WB – metallic W-W bonds, and more covalent W-B and B-B bonds. While we expect the W-W bonds to be the weakest, the relative role played by W-B and B-B bonds in unclear. We first aimed to confirm the anisotropy in strength by calculating the energy shifts in response to small shearing distortions in various directions. As shown in **Fig. 6a**, it is energetically unfavorable to shear *a* (dominated by W-B bonds) along *c*, suggesting that (200) is able to support a large shear stress. In contrast, shearing *b* (which involves the least W-B bonding, but significant B-B bonding) along *c* costs the least energy, suggesting that the (002) might support a lower shear stress, consistent with our experimental results. Note that (020) supports a reasonably high *t*, but plateaus or slips at a fairly low pressure, consistent with the existence of an available slip system (**Fig. 5**). The high *t* value may related to the zigzag topology of the W bilayer, which should strongly resist the propagation of dislocations along the *a* axis.

To understand the high *t* value in the (020) direction in more molecular terms, we again consider W-B bonds. We can identify the bonds that are most active in resisting shear movement by looking at what electronic states are the most energetically affected by geometric distortions.[46] Figure 7b shows the two bonding structures with the highest energy displacements for the (020) plane during shear deformation: both structures are dominated by W-B bonds. To gain further insight into the underlying electronic behavior leading to this strength, we examined the electronic structure of a small model cluster, W_2B_2. The molecular orbitals corresponding to the W-B bonds

shown in **Fig. 6b** are critical to the bond strength. The HOMO-4 is particularly interesting because, in addition to W-B bonding, it corresponds to donation from the d-orbital on W to the σ_{px} bonding orbital in B_2, thereby strengthening the B-B interaction. Hence, the slip between W_2 and B_2 in the cluster disrupts both W-B and B-B bonding. The cluster clearly replicates the bonding patterns seen in the solid, allowing us to conclude that the B-W interaction, rather than B-B bonds, are the cornerstone of the material's strength. This result is interesting because it appears to run counter to the trends in higher borides, where material strength can generally be traced to covalent 2- and 3-D covalent boron networks.

To estimate the macroscopic differential stress (*t*) for polycrystalline sample, one needs to consider the contribution from each diffraction plane. For example, *t* was obtained by taking the average of *t(200)/G*, *t(020)/G* and *t(002)/G* followed by multiplying to obtain the theoretical shear modulus of 198 GPa.[43] Similarly, the differential stress of the LT-tetragonal WB was obtained by using the shear modulus of 199 GPa.[44] The shear modulus at high pressure was extrapolated using *dG/dP* = 1.5, which is a typical value for ceramics.[47] Our hardness tests show that HT-orthorhombic WB is only slightly harder than the LT-tetragonal WB. As seen in **Fig. 7**, the maximum differential stress that the LT and HT materials can support is quite close, with a value of ~11 GPa for both, suggesting that they have a similar macroscopic yield strengths according to Eq. (1), consistent with our hardness measurements. The key difference between HT WB and LT WB

16

appears to lie in their brittleness, as the HT material does not reach a plateau in t until pressures greater than 50 GPa. The differential stress of WB is lower than that of WB_4, but higher than that of ReB_2.[42] Moreover, ReB_2, which is quite brittle, shows a low plateau pressure, similar to the LT WB. By contrast, the HT WB shows a plateau pressure as high as or higher than WB_4.

In addition to looking at differential stress and strain and elastic limits, data collected at the magic angle (54.7°) can be used to calculate the equivalent hydrostatic bulk modulus. The unit cell volume of HT-orthorhombic WB at elevated pressures ranging from 1.7 GPa to 52 GPa is shown in **Fig. 8a**. The compression curve was then fit to the second order Birch-Murnaghan equation-of-state yielding a bulk modulus of 341 ± 5 GPa. This value is in good agreement with recent theoretical predictions[39] for this material. The LT-tetragonal WB was found to be more incompressible than the HT phase with a bulk modulus increased to 381 ± 3 GPa (**Fig. 8b**). We note that this value for the LT tetragonal phase is also in good agreement with theoretical predictions,[15,39,40] but is lower than other measured values.[14,15] Because the orthorhombic phase is only thermodynamically favorable at high temperature, the HT orthorhombic WB is thought to be an entropically stabilized phase. Upon compression, the enthalpy of the LT and HT should be similar because they have fundamentally the same bonding. As a result, the entropy of the HT phase should drop rapidly upon compression, suggesting that HT WB should be more compressible.

In addition to the volume deformation behavior, we also examined the lattice incompressibility. Unexpectedly, the pressure dependence of the fractional lattice constants of HT WB show a discontinuous change in slope, as can be seen in **Fig. S2a**. At pressures lower than ~20 GPa, the a axis is more compressible than the b axis, but upon further compression, the a axis becomes less compressible. Due to the differences in pressure dependence of the lattice constants, it is worth applying an equation-of-state in terms of normalized pressure and Eularian strain[48] to the unit cell parameters, which yields $K_{a(1)}$ = 309 ± 3.5 GPa (using data measured at pressures lower than 20 GPa), $K_{a(2)}$ = 367 ± 3 GPa (using data measured at pressures higher than 20 GPa), K_b = 340 ± 6 GPa and K_c = 324 ± 4 GPa (**Fig. S3a**). It is known that the incompressibility is directly related to the valence electron density.[1] Given that the (020) plane starts to deform plastically at pressures around 15-20 GPa, one possible reason is that the discontinuous increase in directional incompressibility may result from a dislocation induced electronic structure change. There might be a charge density transfer between the W-W bonds and W-B bonds under compression in a similar manner to what has been observed in CrN.[49] For LT WB, the c axis (K_c = 405 ± 2 GPa) was found to be more incompressible than the a axis (K_a = 376 ± 4.5 GPa), which is consistent with the literature.[14]

Conclusions

We have compared the high pressure behavior of WB in two different phases (HT and LT) using synchrotron based X-ray diffraction under non-hydrostatic compression up to ~52 and ~36 GPa, respectively. The bulk modulus for each phase was determined and the LT-tetragonal phase was found to be less compressible than the HT-orthorhombic phase. Moreover, we observed a discontinuous change in directional compressibility in HT-orthorhombic WB. The HT phase of WB shows slightly higher hardness than the LT phase, a result that can be explained by the differential stress data. The LT phase shows slip in both unique symmetry directions at fairly low pressure, indicating multiple accessible slip systems. In contrast, while the (020) plane of the HT WB was found to start slipping at ~15 GPa, the, (200) and (002) planes had not plateaued by 50 GPa, the highest pressures reached in these experiments. Moreover, the (200) plane appears to be the strongest plane that supports the highest differential stress. The two phases were found to support a similar maximum differential stress of ~11 GPa in the pressure range measured, but the LT phase had fully plateaued well before the maximum pressure, while the HT phase was still increasing at our highest pressure, >50 GPa. If we assume that t reflects the lower bound of the yield strength, then these results are consistent with our micro-indentation hardness measurements. Finally, computational studies were used to understand the remarkably high hardness and differential strain observed in these materials, despite their low boron content. The results

19

indicate that for tungsten monoborides, W-B bonds contribute the most to the strength of the material and it is the W-B bonding network that needs to be optimized to increase strength. While lower borides, like WB, are not as hard as higher borides like WB_4, research on lower borides may allow us to optimize the interplay between hardness and brittleness by understanding what controls the available slip systems and how to correlate those features to various bonding motifs.

ACKNOWLEDGMENTS

References:

Captions

FIG. 1. Representative synchrotron X-ray diffraction patterns for (a) the HT phase of WB and (b) the LT phase WB with increasing pressure. Pt diffraction can also been seen, and was included for *in situ* pressure calibration. The crystal structures of orthorhombic HT WB and tetragonal LT WB are shown in parts (c) and (d), respectively.

FIG. 2. Selected *d*-spacings vs. pressure collected at $\varphi = 54.7°$ for HT WB and LT WB. Error bars that are smaller than the size of the symbols have been omitted. Lattice planes were chosen for analysis to define all unique unit cell axes.

FIG. 3. Linearized plots of *d*-spacings for (a) HT WB and (b) LT WB as a function of φ angle at the highest pressure. The solid lines are the best linear fit to the data.

FIG. 4. Part (a) shows the ratio of the differential stress to the aggregate shear modulus (*t(hkl)/G*) for HT WB (black) and LT WB (red). Part (b) shows the evolution of peak broadening for the (020) plane of HT WB and the equivalent (004) plane of LT WB.

FIG. 5. Differential stress (*t*) as a function of pressure for selected lattice planes of HT WB (a) and LT WB (b) under the Reuss (iso-stress) condition (open symbol) and the Voigt (iso-strain) condition (closed symbol). The crystal structure of orthorhombic HT WB looking down the *c* axis and the *a* axis is shown in parts (c) and (d), respectively. The bicolor sticks in these figures denote the W-B bonds.

FIG. 6. Part (a) shows calculated DFT energy changes for HT WB in response to a range of shearing distortions. Part (b) shows relevant bonding structures of the solid.

FIG. 7. Variation of the average differential stress with pressure for HT WB, LT WB, and selected other representative superhard materials.

FIG. 8. Evolution of unit cell volume for HT WB (a) and LT WB (b) as a function of pressure under non-hydrostatic compression. The volume was

measured at $\varphi=54.7°$. Fits (red lines) correspond to the second order Birch-Murnaghan equation-of-state. The insets show the Birch-Murnaghan equation-of-state for WB replotted in terms of normalized pressure and Eulerian strain. The straight line yields the ambient pressure bulk modulus.
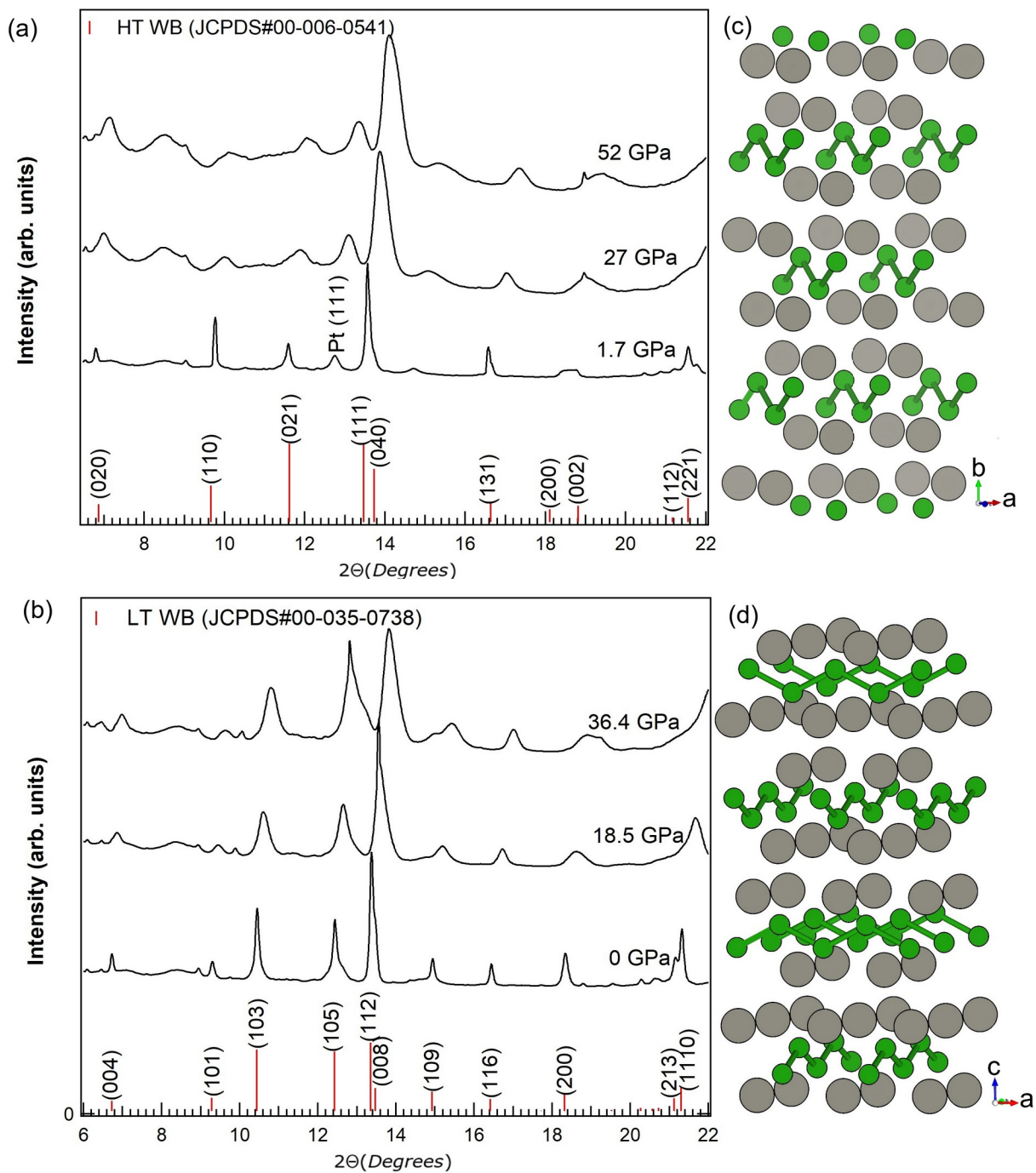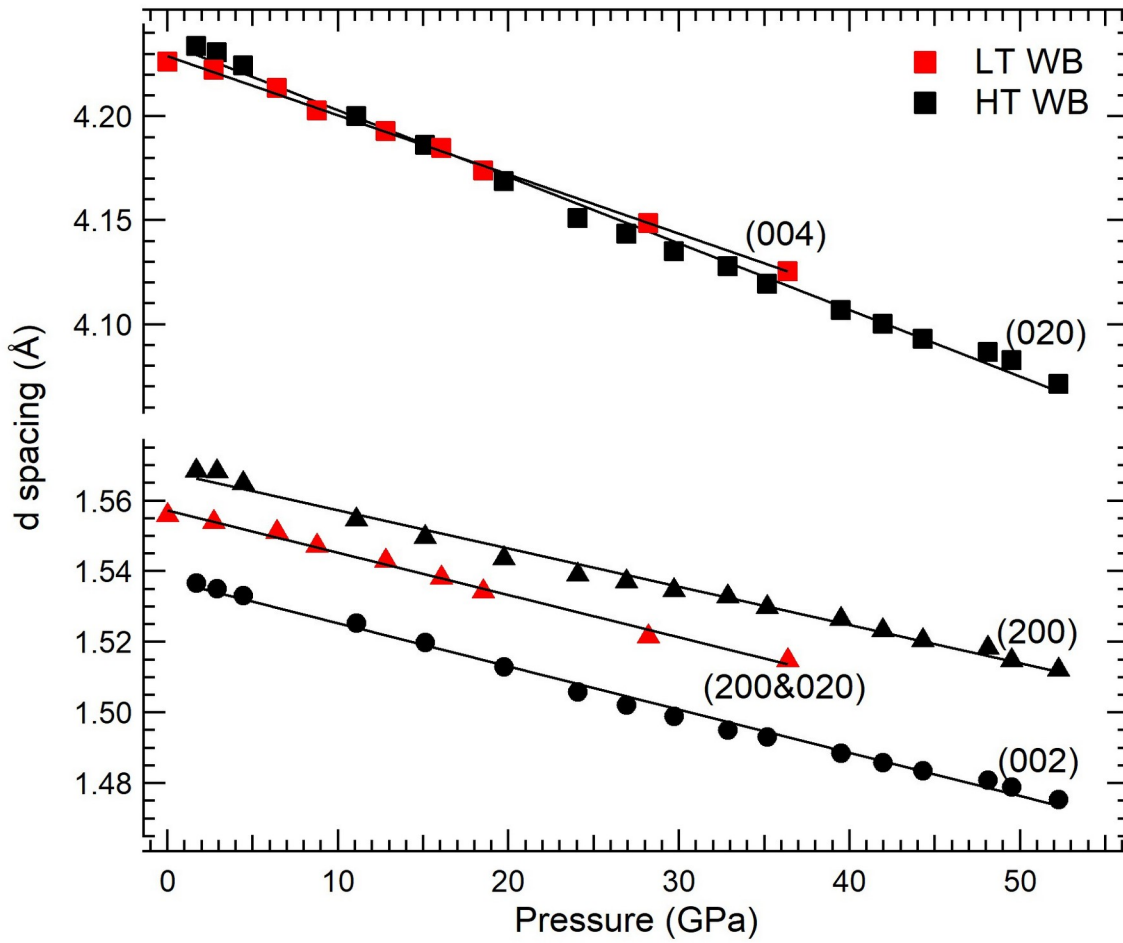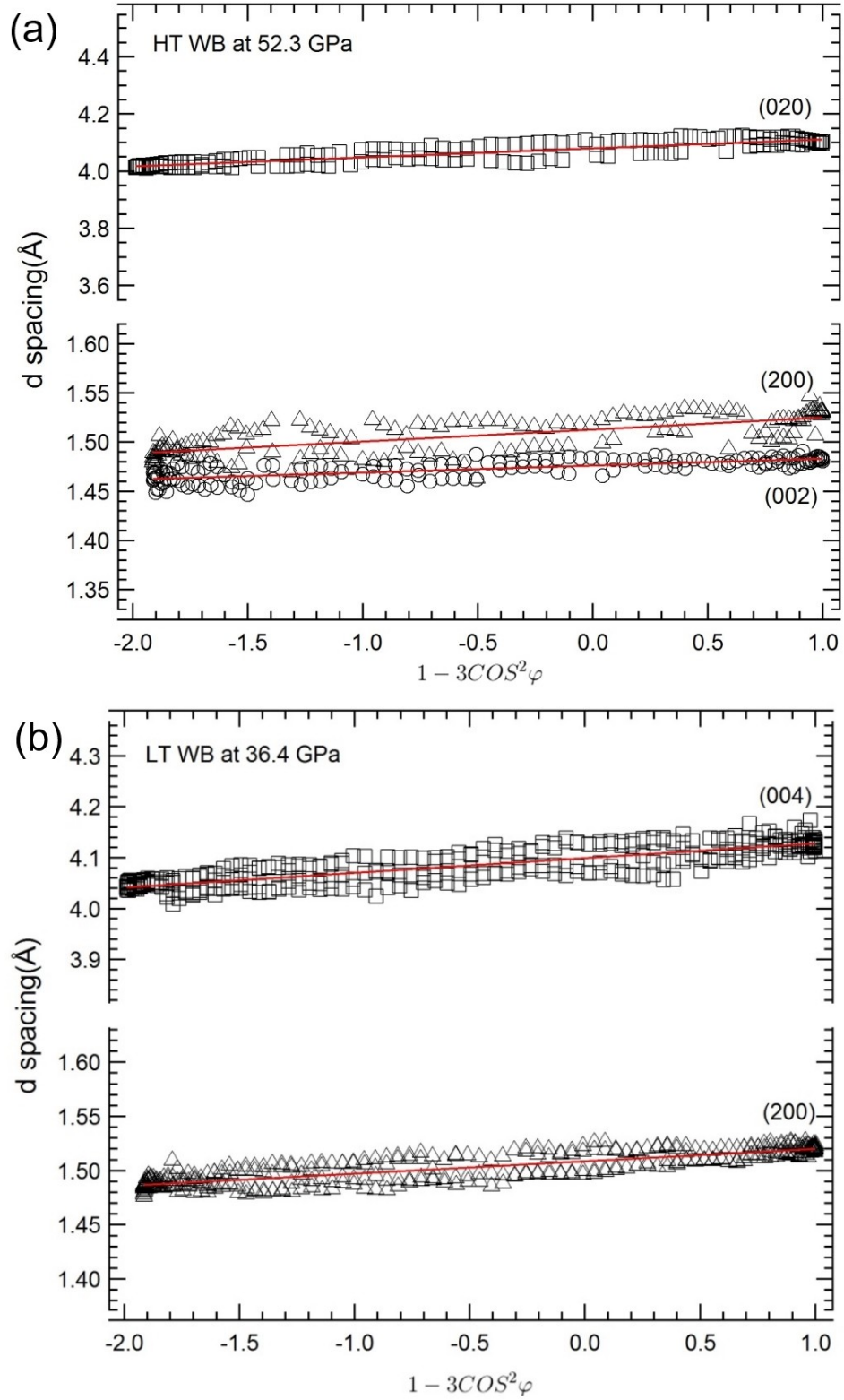
Figures:

FIG. 1.

FIG. 2.

(a) HT WB at 52.3 GPa

(020)

(200)

(002)

$1 - 3COS^2\varphi$

(b) LT WB at 36.4 GPa

(004)

(200)

$1 - 3COS^2\varphi$

FIG. 3.

FIG. 4.

(a)

t_Voigt(200)
t_Reuss(200)
t_Voigt(020)
t_Reuss(020)
t_Voigt(002)
t_Reuss(002)

HT WB

(b)

t_Voigt(004)
t_Reuss(004)
t_Voigt(200)
t_Reuss(200)

LT WB

(c)

(d)

FIG. 5.

(a)

(b)

W$_2$B$_2$

1.65 Å

W(d) → B-B(σ_{2px})

W(d) → B-B(π*)

HOMO-4

HOMO-1

HOMO-2

FIG. 6.

FIG. 7.

(a)

Second-order Birch-Murnaghan EOS
$K_0 = 341 \pm 5$ GPa
Fixed $K'_0 = 4$
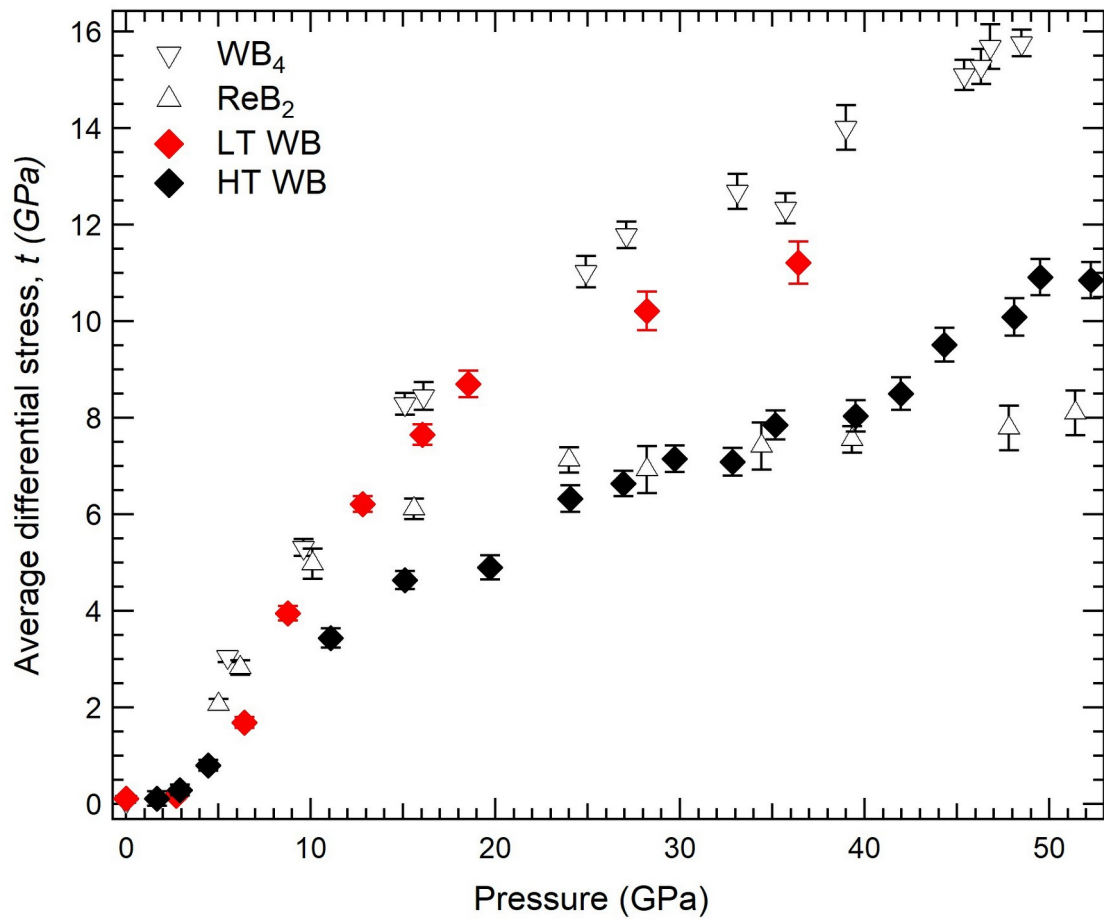
(b)

Second-order Birch-Murnaghan EOS
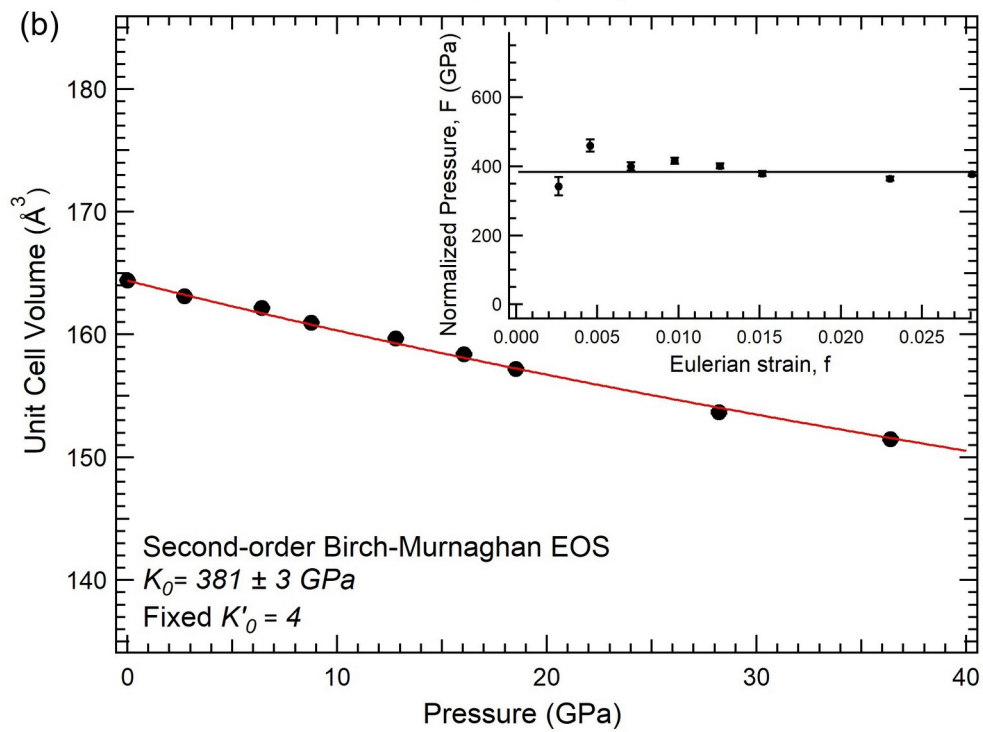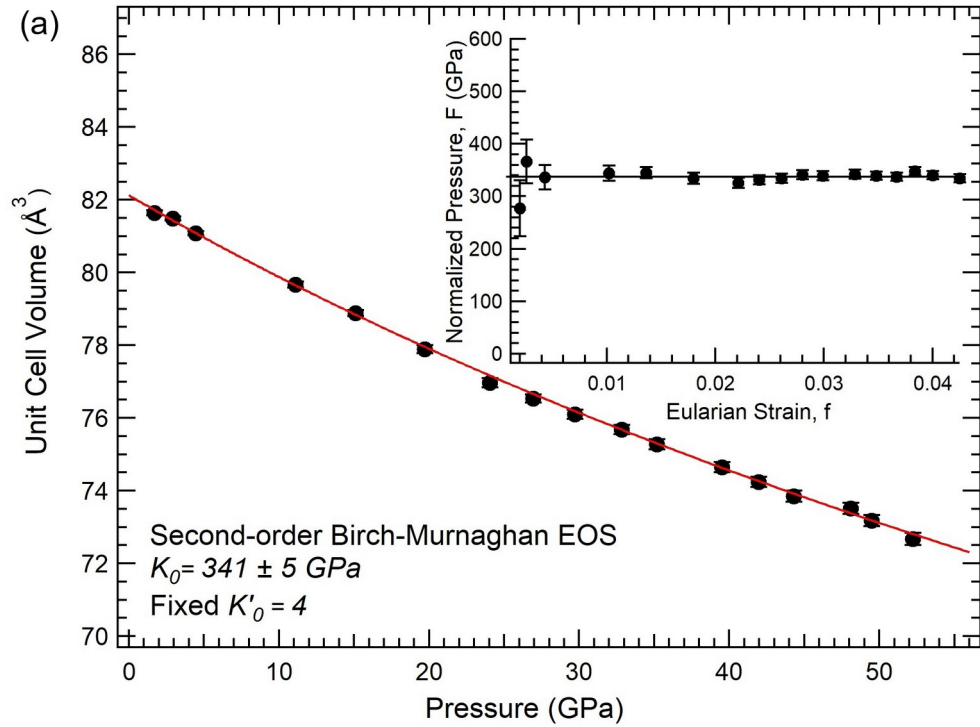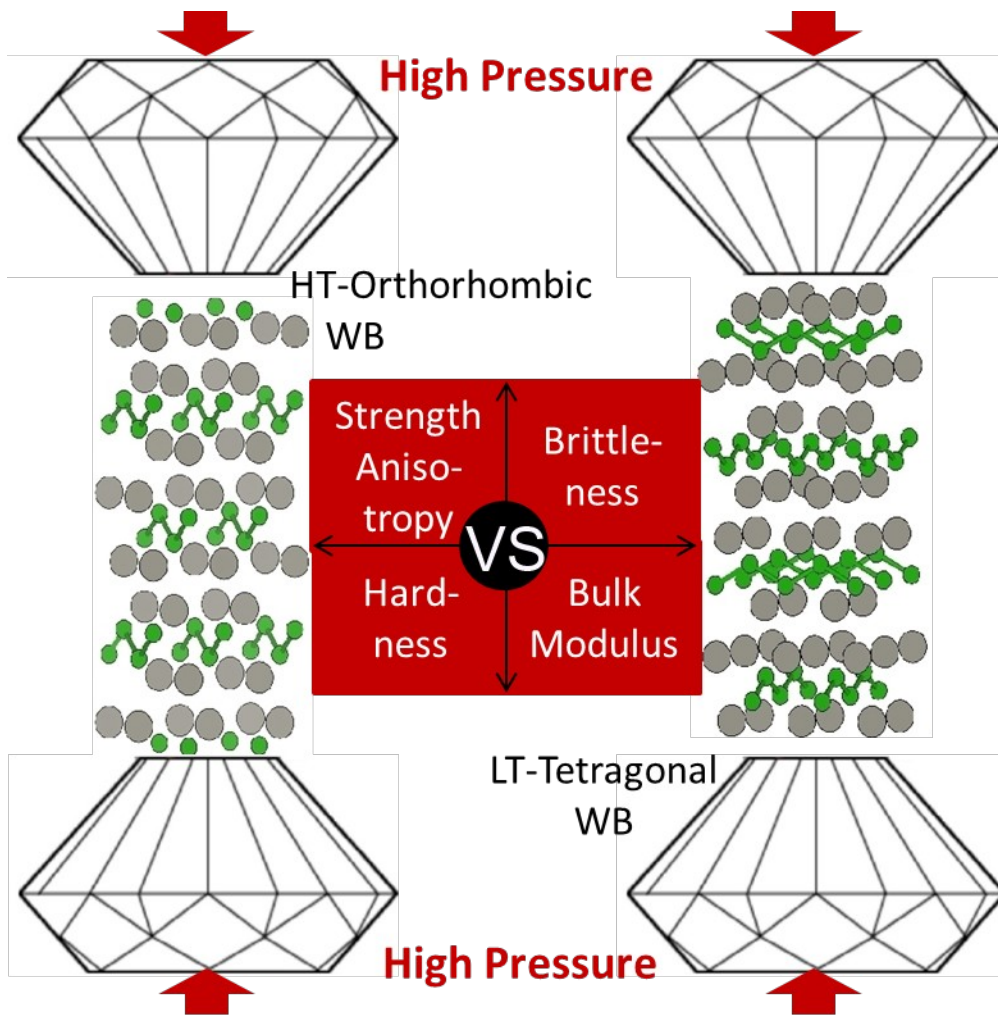$K_0 = 381 \pm 3$ GPa
Fixed $K'_0 = 4$
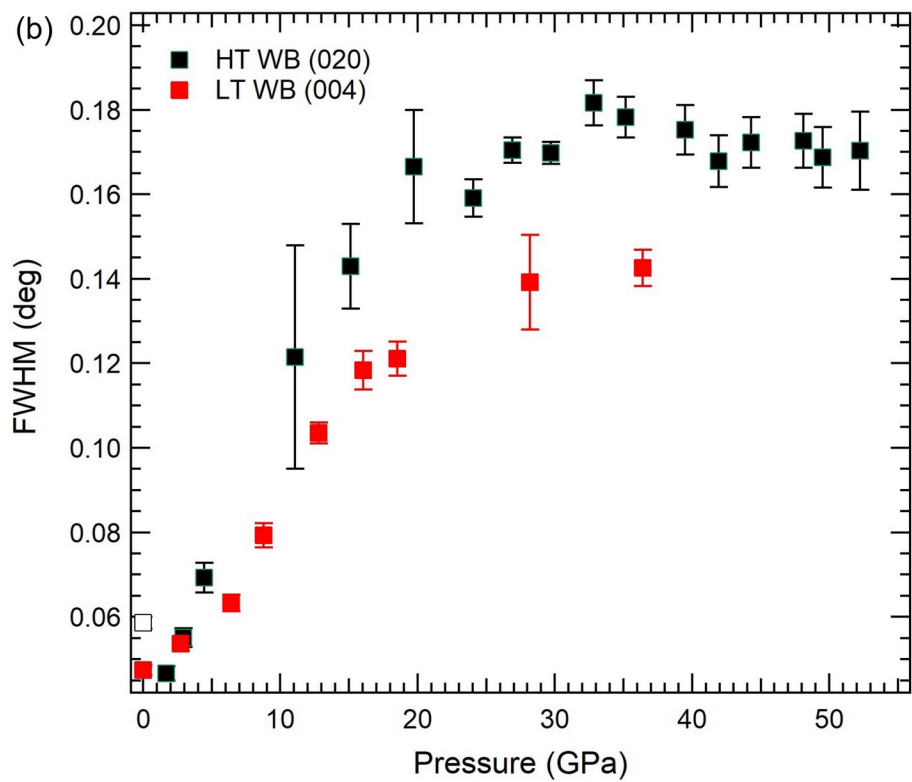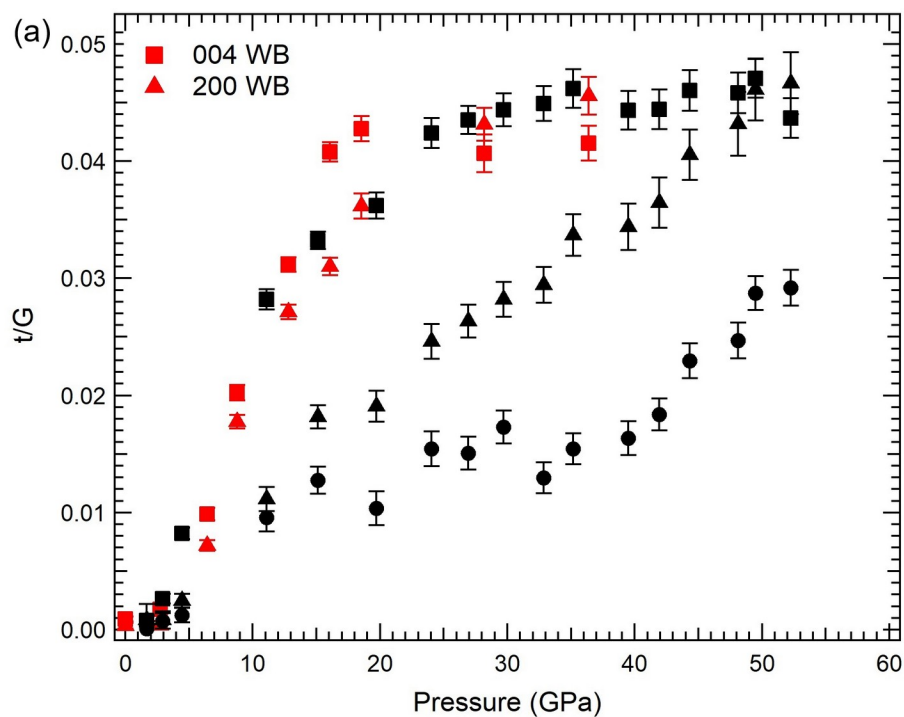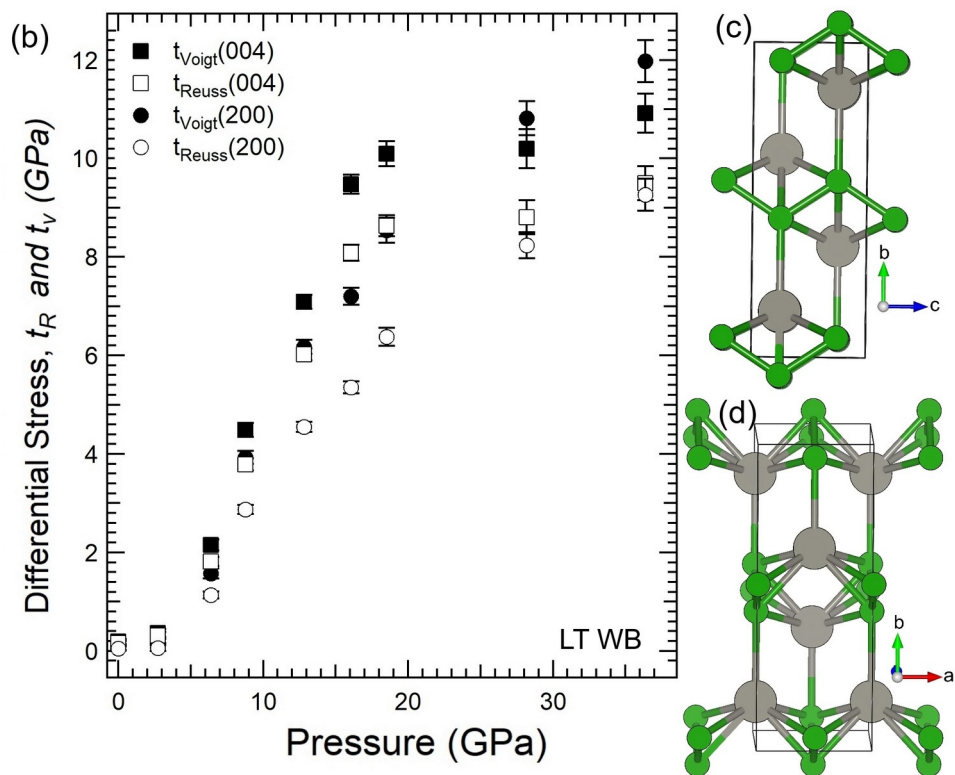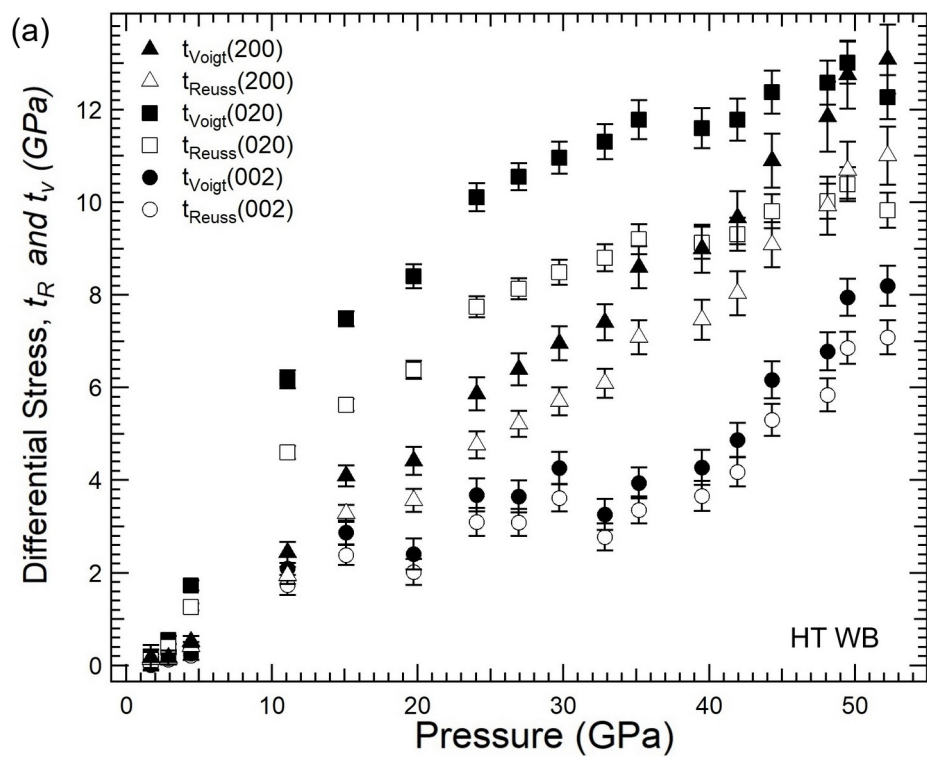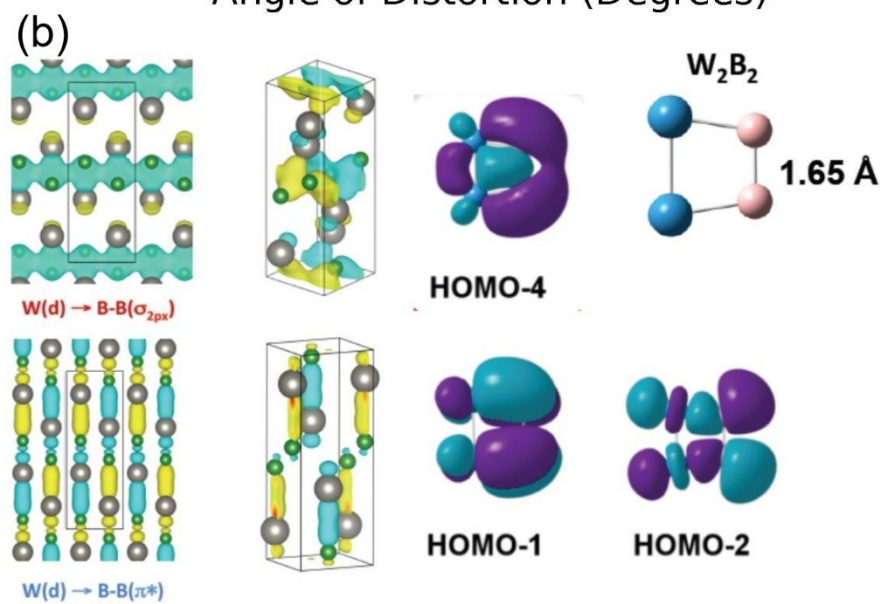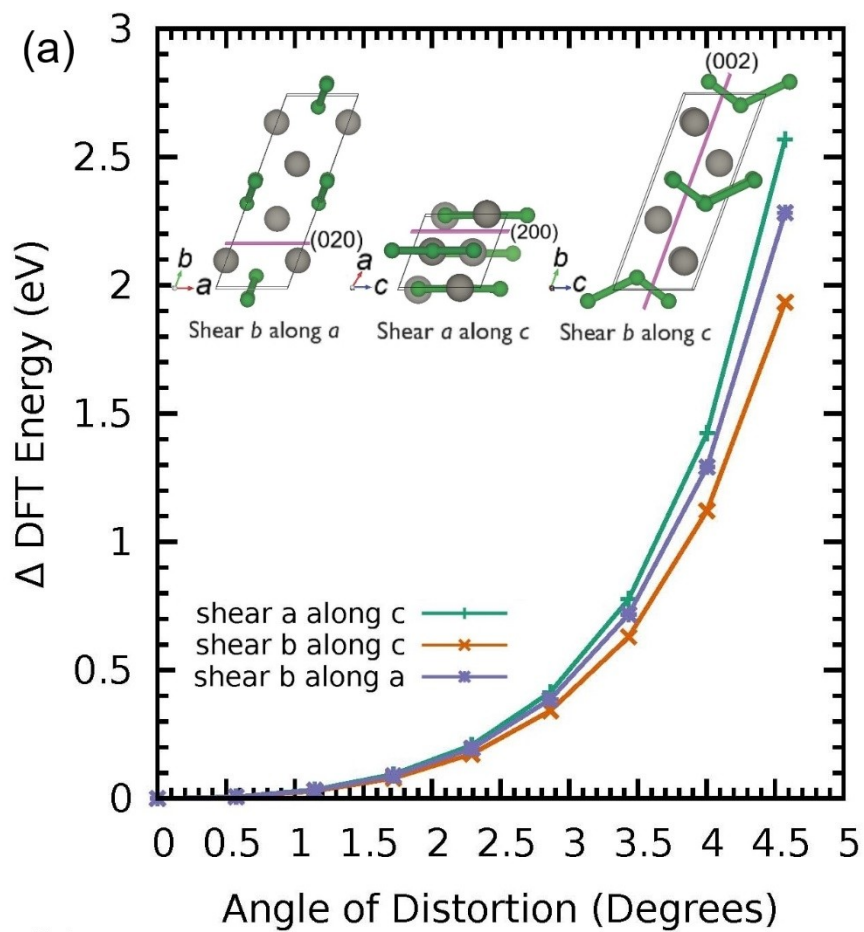
FIG. 8.

TOC Graphic:

1   J.B. Levine, S. H. Tolbert, and R. B. Kaner, Adv. Funct. Mater. **19**, 3519 (2009).

2   R. Komanduri, and M. C. Shaw, Nature (London) **255**, 211 (1975).

3   A. Kavner, M. B. Weinberger, R. B. Kaner, and S. H. Tolbert, J. Appl. Phys. **112**, 013526 (2012)

4   H.-Y. Chung, M. B. Weinberger, J. B. Levine, A. Kavner, J.-M. Yang, S. H. Tolbert, and R. B. Kaner, Science **316**, 436 (2007).

5   T. Taniguchi, M. Akaishi, and S. Yamaoka, J. Am. Ceram. Soc. **79**, 547 (1996).

6   R.Mohammadi, A. T. Lech,M. Xie, B. E.Weaver, M. T. Yeung, S. H. Tolbert, and R. B. Kaner, Proc. Nat. Acad. Sci. **108**, 10958 (2011).

7   R. Mohammadi, M. Xie, A. T. Lech, C. L. Turner, A. Kavner, S. H. Tolbert, and R. B. Kaner, J. Am. Chem. Soc. **134**, 20660 (2012).

8   M. Xie, R.Mohammadi, Z.Mao,M.M. Armentrout, A. Kavner, R. B. Kaner, and S. H. Tolbert, Phys. Rev. B **85**, 064118 (2012).

9   P.A. Romans and M. P. Krug, Acta Crystallogr. **20**,313 (1966).

10 R.Mohammadi, C. L. Turner, M. Xie, M. T. Yeung, A. T. Lech, S. H. Tolbert, and R. B. Kaner, Chem. Mater. **28**, 632 (2016).

11 A. T. Lech, S. H. Tolbert, and R. B. Kaner *el al.,* Proc. Nat. Acad. Sci. USA **112**, 3223 (2015).

12 H. Duschanek, and P. Rogl, J. Phase Equilib. **16**, 150 (1995).

13 M. T. Yeung, R. Mohammadi and R. B. Kaner, Annu. Rev. Mater. Res. **46**, 1 (2016).

14 H. Dong and T. S. Duffy et al., J. Appl. Phys. **111**, 123514 (2012)

15 C. Fan, C. Liu, F. Peng, N. Tan, M. Tang and J. Liu et al., Physica B **521**, 6 (2017).

16 M. T. Yeung, J. Lei, R. Mohammadi, Y. Wang, S. H. Tolbert and R. B. Kaner, Adv. Mater. **28**, 6993 (2016)

17 R.J. Hemley, H.K. Mao, G. Shen, J. Badro, P. Gillet, M. Hanfland and D. Häusermann, Science, **276**, 1242 (1997).

18 H. K. Mao, J. F. Shu, G. Y. Shen, R. J. Hemley, B. S. Li, and A. K. Singh, Nature (London) **396**, 741 (1998).

19 S. Merkel, J. Phys. Condens. Matter. **18**, 949 (2006).

20 T. S. Duffy, AIP Conf. Proc. **955**, 639 (2007).

21 E. H. Yoffe, Philosophical Magazine A, **46**, 617 (1982).

22 S. Merkel and T. Yagi, Rev. Sci. Instrum. **76**, 046109 (2005).

23 S. Merkel, H. R. Wenk, J. Shu, G. Shen, P. Gillet, H. K. Mao, and R. J. Hemley, J. Geophys. Res. **107**, 2271 (2002).

24 A. P. Hammersley, S. O. Svensson, M. Hanfland, A. N. Fitch, and D. Hausermann, High Pressure Research **14**, 235 (1996).

25 A. K. Singh, H.-K. Mao, J. Shu, and R. J. Hemley, Phys. Rev. Lett. **80**, 2157 (1998).

26 A. K. Singh, J. Appl. Phys. **73**, 4278 (1993).

27 A. K. Singh, C. Balasingh, H.-K. Mao, R. J. Hemley, and J. Shu, J. Appl. Phys. **83**, 7567 (1998).

28 A. L. Ruoff, J. Appl. Phys. **46**, 1389 (1975).

29 A. K. Singh, J. Appl. Phys. **106**, 043514 (2009).

30 A. Reuss, Z. Angew. Math. Mech. **9**, 49 (1929).

31 W. Voigt, *Lehrbuch der Kristallphysik* (Teubner, Leipzig, 1928).

32 R. F. S. Hearmon, Adv. Phys. **5**, 323 (1956).

33 G. M. Amulele, M. H. Manghnani, and M. Somayazulu, J. Appl. Phys. **99**, 023522 (2006).

34 D.W. He, S. R. Shieh, and T. S. Duffy, Phys. Rev. B **70**, 184121 (2004).

35 F. Birch, J. Geophys. Res. **83**, 1257 (1978).

36 T. Egami, Y. Waseda, J. Non-Cryst. Solids, **64**, 113 (1984).

37 Y. Fei, A. Ricolleau, M. Frank, K. Mibe, G. Shen, and V. Prakapenka, Proc. Nat. Acad. Sci. USA **104**, 9182 (2007).

38 L. Han, S. Wa, and C. Jin et al., Appl. Phys. Lett. **106**, 221902 (2015).

39 Y. Liang, Z. Gao, P. Qin, L. Gao and T. Chun, Nanoscale, DOI: 10.1039/C7NR02377D (2017).

40 B. Chen, K. Lutker, S. V. Raju, J. Yan, W. Kanitpanyacharoen, J. Lei, S. Yang, H.-R. Wenk, H.-K. Mao and Q. Williams, Science, **338**, 1448 (2012).

41 D. J. Weidner, Y. Wang, and M. T. Vaughan, Science **266**, 419 (1994).

42 M. Xie, R. Mohammadi, C. L. Turner, R. B. Kaner, A. Kavner, and S. H. Tolbert, Phys. Rev. B **90**, 104104 (2014)

43 Y. C. Liang, Z. Zhong, and W. Q. Zhang, Comput. Mater. Sci. **68**, 222 (2013).

44 X.-Y. Cheng, X.-Q Chen, D.-Z. Li and Y.-Y. Li, Acta. Crystallogr. **70**, 85 (2014).

45 M. Hebbache, Solid State Commun. **113**, 427 (2000).

46 P. J. Robinson and A. N. Alexandrova, J. Phys. Chem. A **119**, 12862 (2015).

47 D. G. Isaak, *Handbook of Elastic Properties of Solids, Liquids, and Gases* (Academic Press, San Diego, CA, 2001).

48 C. Meade and R. Jeanloz, Geophys. Res. Lett. **17**, 1157 (1990).

49 F. Rivadulla, M. Bañobre-López, J. B. Goodenough, Nature Mater*.* **8,** 947(2009).